RSC Advances

ROYAL SOCIETY OF CHEMISTRY

www.rsc.org/advances

Lateral heterojunctions within monolayer h-BN/Graphene: a First-principles study

Qilong Sun, Ying Dai*, Yandong Ma, Wei Wei and Baibiao Huang

School of Physics, State Key Laboratory of Crystal Materials, Shandong University

Jinan 250100, P. R. China

Abstract

Very recently, the lateral heterojunctions of hexagonal boron nitride (h-BN)/graphene were first realized experimentally. To study the related properties of such heterojunction with the purpose of searching for new avenues to realize controllable and tunable 2D electric devices, in the present work, we perform a systematical theoretical investigation on a series of structures constructed by zigzag h-BN and zigzag graphene monolayers based on first-principles calculations. Our results demonstrate that the electronic structures as well as the magnetic properties of the hybridized monolayers can be modified efficiently. Furthermore, the character transition from insulator to metal can also be realized by the proposed approaches of adjusting the numbers or the ratios of the zigzag h-BN and zigzag graphene. Interestingly, research of the strain dependence of the electronic properties in the selected structure reveals that the external strain applied along the Y-axis plays a decisive role in the bandgap engineering. Moreover, the calculated effective masses give a reasonable physical representation of the carriers transport properties. Our results show that the mobility direction of the charge carriers is parallel to the interface. These predications provide new potential strategies for turning electronic

* E-mail: daiy60@sina.com

properties and will allow new device functionalities, such as in-plane transistors, diodes and spintronic devices to be integrated within a single thin layer.

Keywords: first-principles; graphene; BN; heterojunction; strain; monolayer; two dimensional materials

1 Introduction

Since its discovery[1], graphene has attracted widespread interests in the literature[2-5] due to its unique structural, electrical and mechanical properties.[6-8] Graphene has become an ideal candidate for numerous applications in the next generation of electronic devices. Subsequently, many other two-dimensional (2D) materials, including BN, silicene and MoS_2, have also been theoretically predicted or experimentally fabricated.[9-12] Among them, the BN monolayer received particular attention as it holds distinct properties as compared with graphene. For example, unlike graphene composing of two equivalent sublattices of C atoms, the B and N atoms in BN monolayer form chemically nonequivalent ones in the honeycomb lattice, which give raise to a wide-gap of ~5.5 eV.[13, 14] Besides, BN monolayer own nearly flat band structure in the whole first Brillouin zone, while graphene is a strictly zero bandgap semiconductor, processing linear dispersive bands near the Fermi level forming a perfect Dirac cone, contrastingly.[15-17]

When considering the application in the future electronics, controlled ways for realizing the completely tunable electronic and magnetic properties are highly desirable. Up to now, some methods have been developed, including chemical decorated, hydrogen-terminated, applying an external strain, and so on.[18-21] As we

know, Heterostructures between three-dimensional (3D) semiconductors with different bandgaps are the basis of modern light-emitting diodes, diode lasers and high-speed transistors. Lately, creating analogous heterostructures between different 2D materials, which can enable band engineering within the 2D plane, has opened up new realms in materials science, device physics, and engineering.[22-25] Considering the optimized lattice constants which differ less than 2%, the 2D graphene and h-BN would be the best candidates to fabricate the lateral heterostructures in monolayer materials. The first pioneering experiment was performed by Ci et al., who obtained few layer films with randomly distribution graphene and h-BN domains on Cu foils and observed a small bandgap of 18meV.[26] Subsequently, Liu et al. synthesized a quasi-freestanding in-plane h-BN/graphene heterostructure on a weakly coupled Ir (111) single crystal surface.[27] They also found that most boundaries are of zigzag type with no atomic mix. With these works in mind, some interesting questions then arise: how to further engineer the bandgaps and electronic properties of the 2D heterostructures monolayers, as the hybridized configurations is feasible in the experiments. Is there any possibilities that the transition from insulators through semiconductors to conductors can be implemented in the lateral heterojunctions consisted of h-BN.

Inspired by those questions, in the present work, we proposed a theoretical method to realize the bandgap engineering by gradually adjusting the numbers and ratios of zigzag-graphene monolayer (denoted as ZGM) and zigzag-h-BN monolayer (denoted as ZBNM). And this strategy is expected to open a new route to tailor bandgaps in 2D

materials. Here, using first-principles calculations, we performed a detailed analysis of changes in structural as well as electronic and magnetic properties of the hybridized in-plane structures. Our results reveal that all of the hybridized structures show an ideal planar nature without any distortions. The transition from insulator to semiconductor, and to metal is realized by varying the numbers or ratios of the ZBNM and ZGM units, which are used to fabricate the in-plane heterostructures. Most importantly, the bandgap of the hybridized monolayers can be tuned efficiently by either adjusting the numbers of ZBNM and ZGM with the same ratios or changing the ratios of the different units. Additionally, we also find that the fundamental band gap can be continuously driven by the strain effect applied along the Y-axis. Furthermore, the calculated effective mass reveals the transfer direction of the carriers, tending to be parallel to interface.

2 Computational methods

The first-principles calculations are performed by density functional theory (DFT) in conjunction with projector augmented wave (PAW) potentials, which is implemented in the Vienna ab initio simulation package (VASP).[28, 29] For the exchange-correlation functional, the generalized gradient approximations (GGA) of Perdew–Burke–Ernzerhof (PBE) is used.[30] The periodic in-plane hybridized monolayers are optimized within one repeating unit. We applied periodic boundary conditions and a vacuum space of 15 Å along the z direction in order to avoid the interactions between two slabs in the nearest-neighbor unit cells. A cutoff energy of 450eV is used for the plane wave expansion of the wave function to converge the

relevant quantities. The Monkhorst-Pack scheme of k point sampling is used for integration over the first Brillouin zone. A 25×3×1 grid for k-point sampling is used for geometry optimization and the static total energy calculations.[31] All structures are fully optimized until the residual forces are less than 0.01 eV/Å. The convergence criteria for energy of 10^{-5} eV is met.[32]

3 Results and discussion

For the in-plane heterostructures of the h-BN and graphene, it could be classified into two types: the hybridized configurations with the same ratios of ZBNM and ZGM units; and the ones with different ratios of the two systems. For the convenience of our discussion, we denote those two types of configurations as $(ZBNM)_m$-$(ZGM)_n$, where the *m* and *n* define the numbers of ZBNM and ZGM units, respectively. The unit cells used in the study of the in-pane heterostructures fabricated by h-BN and graphene with zigzag interfaces are depicted in Figure 1. Here, it should be noted that due to the periodic boundary conditions used in these calculations, we effectively have alternating domains of graphene and h-BN in the direction perpendicular to the interface. Now, we first consider the configurations of $(ZBNM)_m$-$(ZGM)_n$ with $m = n$. In order to simulate the in-plane heterostructures with different widths, we built the monolayers of $(ZBNM)_m$-$(ZGM)_n$ by gradually increasing $m = n$. In detail, we have investigated the hybridized monolayers including the $(ZBNM)_m$-$(ZGM)_n$ with the $m = n$ = 2, 4, 6, 8, 10, 12, 14, and 16, respectively. On the other hand, for the cases of hybridized configurations with the different ratios of ZBNM and ZGM units ($m \neq n$), we have studied the properties of $(ZBNM)_2$-$(ZGM)_{18}$, $(ZBNM)_4$-$(ZGM)_{16}$,

$(ZBNM)_6$-$(ZGM)_{14}$, $(ZBNM)_8$-$(ZGM)_{12}$, $(ZBNM)_{12}$-$(ZGM)_8$, $(ZBNM)_{14}$-$(ZGM)_6$, $(ZBNM)_{16}$-$(ZGM)_4$, and $(ZBNM)_{18}$-$(ZGM)_2$. After fully relaxed, we find that all of the considered structures in this work have an ideal planar nature without any distortion, which are similar to the pristine graphene. In addition, both of the ZBNM and ZGM units have maintained the structural properties of the honeycomb lattice with a complete sp^2 hybridization. For the isostatic configurations ($m = n$), the relaxed C-N bond lengths between the linked ZBNM and ZGM units are elongated slightly when the numbers of the different units increase from 2 to 16. Therefore, it can be concluded that the width of the hybridized unites in the monolayer has limited influence on the bonding strength of the interfaces. Moreover, we find that the configurations with different ratios of ZBNM and ZGM units share similar geometric structures with the $(ZBNM)_{10}$-$(ZGM)_{10}$, implying that various ratios of the hybridized units will not cause any defects in the 2D heterostructures.

As we know, band gap engineering is a powerful technique and an essential part of nanoelectronics and nanophotonics. Recent advances in engineering the band gap of 2D materials motivate us to study how to tune the band gap of the technologically important 2D in-plane lateral heterostructures. Now an interesting question arises as to whether the various widths or ratios of the hybridized ZBNM and ZGM unites would play a role in the bandgap engineering for the whole monolayer? To answer this question, it is thus necessary to study the electronic properties of the selected in-plane heterostructures. Firstly, we examine the influence of different widths on the in-plane heterostructures. The calculated electronic band structures for

$(ZBNM)_2$-$(ZGM)_2$, $(ZBNM)_4$-$(ZGM)_4$, $(ZBNM)_6$-$(ZGM)_6$, $(ZBNM)_8$-$(ZGM)_8$, $(ZBNM)_{10}$-$(ZGM)_{10}$, $(ZBNM)_{12}$-$(ZGM)_{12}$, $(ZBNM)_{14}$-$(ZGM)_{14}$, and $(ZBNM)_{16}$-$(ZGM)_{16}$ are depicted in Figure 2(a) – 2(h) respectively. As shown in Figure 2(a), there is an optical direct bandgap of the $(ZBNM)_2$-$(ZGM)_2$ near the Y high symmetry points, yielding a band gap of 1.19 eV. Besides, we note that the electronic band structures display symmetric characteristic for the majority and minority projections of the spin. At this points, clearly, the 2D hybridized $(ZBNM)_2$-$(ZGM)_2$ is nonmagnetic. Further, a notable lack of particle-hole symmetry could be identified easily in the band structures, which is partly due to the different potentials between B and N site. In addition, due to the ionic B-N bonds a fundamental gap of about 4.6 eV is opened at the Γ points. Therefore, forming heterostructures between these 2D systems, graphene and BN, the BN stripes will form potential barriers for electrons and holes in graphene. For the $(ZBNM)_4$-$(ZGM)_4$, and $(ZBNM)_6$-$(ZGM)_6$, as shown in the Figure 2(b) and 2(c), the bandgaps are greatly reduced to 0.14 eV and 0.01 eV, respectively. Here, our calculations reveal that the widths of hybridized ZBNM and ZGM units with the same ratio play an important role in the bandgap engineering. With increasing the number of the units, the bandgap will decrease monotonically. Moreover, regarding to the magnetic properties of $(ZBNM)_4$-$(ZGM)_4$, and $(ZBNM)_6$-$(ZGM)_6$, similar results could be obtained compared to the $(ZBNM)_2$-$(ZGM)_2$, and the total magnetic moments are zero, indicating the local magnetic moments cannot form in the 2D hybridized $(ZBNM)_m$-$(ZGM)_n$ with $m = n < 6$. All results are summarized in Table 1 (Col^a).

However, as shown in Figure 2(d), we can see clearly that the electronic band structures of the majority and minority projections states are separated near the Fermi level, when $m = n$ increases to eight. Meanwhile, both of the two bands cross the Fermi level, which shows the $(ZBNM)_8$-$(ZGM)_8$ system is metallic. When further increasing the number of the hybridized ZBNM and ZGM units simultaneously, the natures of metal are still maintained and the band structures are of very small change while the majority and minority projections states only leave tiny gaps about 10 meV, as shown in Figure 2(e) – 2(h). Thus, the $(ZBNM)_{16}$-$(ZGM)_{16}$, which own the lattice constants b = 6.9 nm, is sufficient to simulate the 2D in-plane heterostructures compared to the experiments results mentioned previously. It is noteworthy that the energy bands of majority and minority states are also asymmetric near the Fermi level, indicating spin polarization occurs in those systems with the indexing $m = n > 8$. Further, our calculations reveal that the spin-polarized configurations are more stable than their corresponding non-polarized states with the energy differences being about 1-3 *meV*. It should be noted here, for wider systems, the edge states give rise to a narrow band near the Fermi level, enabling the possibility of magnetic orderings induced by the electron-electron interaction. So far, our results show that the transitions from insulator (h-BN) through semiconductor, to metal have been induced by increasing the numbers of ZBNM and ZGM units with the same ratio. On the other hand, it can be concluded that the metal behavior of $(ZBNM)_m$-$(ZGM)_n$ mainly originates from the hybrid connection of ZBNM and ZGM units.

To understand this interesting magnetic properties in more detail, taking the

$(ZBNM)_{10}$-$(ZGM)_{10}$ as an example for simplicity, we plot the top and side views of the spin density in Figure 3. The calculated spin density distributions for $(ZBNM)_{10}$-$(ZGM)_{10}$ reveal that the magnetic moments are strongly localized at the zigzag edges, arranging themselves ferromagnetic along a particular edge. The spin-polarized atoms only extend to the region of BN_1 and C_{1-3} units as shown in Figure 3. It can be found that the zigzag graphene and h-BN have similar magnetic orientations (shown in Figure 3a), and the spin mainly originated from the corresponding P_Z orbitals as shown in Figure 3(b). Furthermore, the minority (majority) spin density states are mostly localized at the C atom, making an interface with N (B), at the two opposite boundaries of the graphene. Bhowmick et al. reported similar magnetic properties for zigzag graphene nanoroads embedded in h-BN, where the nanoroads of graphene process spin-polarized edges.[33, 34] Our results also validate their previous findings. Moreover, the existence of the interface-localized state have been identified in the experiment.[35]

On the other hand, strain effects caused by radial size are always important in nanosystems. Previous studies[36-40] indicated that strain on nanosystem can change their electronic structures remarkably and thus provides a dimension for nanoelectronic engineering. Considering strain can be readily exerted on nanosheets either intentionally or naturally while the strain engineering has been identified to be also efficacious for single layers, we propose here to tune the bandgaps on the 2D in-plane heterostructures through strain engineering. Thus, we investigate the strain dependence of the geometric and electronic structures in semiconducting

$(ZBNM)_2$-$(ZGM)_2$ by varying the isotropic strain from -10% to 10% in which both the overall honeycomb-like structures and the crystal symmetries are all maintained. It is worth pointing out that this strain range does not exceed the mechanical strength.[39] The tensile or compression strain is uniformly applied along the X-axis and Y-axis directions as shown in the inset of Figure 4. The isotropic strain is defined as $\varepsilon = \Delta c/c_0$, where the lattice constants of the unstrained and strained supercell equal to c_0 and $c = \Delta c + c_0$, respectively.[41, 42] The stretching or compressing of the $(ZBNM)_2$-$(ZGM)_2$ monolayer is achieved by first elongating the optimized lattice constant c_0 to $c = \Delta c + c_0$ and uniformly expanding the atomic structure obtained from previous optimization. Subsequently, the atomic structure is reoptimized and the corresponding bandgap is calculated with the elongated lattice constant fixed.

For the semiconducting $(ZBNM)_2$-$(ZGM)_2$ monolayer in Figure 4 (the black line) it is shown how, upon strain, the bandgap varies as a function of the applied uniaxial strain. It should be noted that the bandgap increases monotonically with increasing tensile strain up to -10%, and on the contrary, the bandgap decreases monotonically with decreasing compressive strain up to 10%. Obviously, the relationship between the strain and bandgap is predicted to be a nearly linear response. As known to all, the strain for sp^2 bond breaking in graphene is 18%, thus this strain is feasible as a reversible control as mentioned previously.[43] Secondly, it is found that the variation of the bandgap according to the strain is significant within a large range of 0.9 eV, which is almost 90% compared to primary bandgap. Thus our results demonstrate that the strain effect is an effective way for the bandgap modulation in $(ZBNM)_2$-$(ZGM)_2$.

Moreover, note that the projected density of states of hybridized configuration (not shown here) shows an increased contribution from C- P_Z orbitals in forming the upper valence band with the increase of strain. Consequently, we could obtain the $(ZBNM)_2$-$(ZGM)_2$ monolayer with continuous and precisely bandgaps modified by the applied mechanical strains, which may have enormous potential applications in photocatalysis, electrical device and so on. Next, in order to identify the origin of the strain-induced variations of the bandgap, we also examine the effect of uniaxial strain as shown in Figure 4, where the green (red) lines correspond to the relationship between the strain applied along the X-axis (Y-axis) and the calculated bandgaps. We find that the strain, which is parallel to the interface, has very limited influence on the bandgap (about 0.03 eV). Meanwhile, for the case of the strain applied along the Y-axis, the variation of the bandgap is up to 0.9 eV which is similar to the cases applied biaxial strain. However, it is also found that the variation of the bandgap is minor as the ε increase from 8% to 10%. Thus, further compressive strain ($\varepsilon > 10\%$) would not have an effective influence on the bandgap anymore. So that, it is concluded that the strain applied along the Y-axis plays a vital role in the bandgap engineering. In other words, the bonds between the connected C and N dominate the electronic properties of the 2D heterostructure. Explanation of this interesting change is sought in the fact that, the strain impact not only the sp^3 characteristic, but also the width of the sandwich structures, which has been mentioned before.

Further, the carrier effective mass could present a uniform description of the ability to transfer electron-holes along special directions, which is important to carrier

transfer related properties such as mobility of nanosystem. Therefore, the effective masses of electrons (m_e^*) and holes (m_h^*) along various directions are discussed and calculated by fitting parabolic functions to conduction band minimum (CBM) and valence band maximum (VBM) of the $(ZBNM)_2$-$(ZGM)_2$ according to the Equation (1):

$$m^* = \pm\hbar^2\left(\frac{d^2E_k}{dk^2}\right)^{-1} \quad (1)$$

where k is the wave vector, and E_k is the energy corresponding to the wave vector k. The direction along the $(\Gamma \rightarrow Y)$ and the other two directions which make 45° and 60° angle with the $(\Gamma \rightarrow Y)$ are selected, respectively, to give a qualitative study of the mobility of the 2D $(ZBNM)_2$-$(ZGM)_2$ material. In view of the symmetry of the 2D structure, these three directions, which are denoted as $(\Gamma \rightarrow Y)^0$, $(\Gamma \rightarrow Y)^{45}$ and $(\Gamma \rightarrow Y)^{60}$, are sufficient and reasonable to describe the properties of the carriers transfer. The region for parabolic fitting was within an energy difference of 10 meV around the CBM or VBM, which gave quite reasonable results compared to other theoretical and experimental results.[44] The results are summarized in Table 2. It can be seen that the electron effective masses of $(ZBNM)_2$-$(ZGM)_2$ increase monotonically while the deviation from the direction of $(\Gamma \rightarrow Y)$ turns large. The effective messes of electrons are $0.65\,m_e$, $0.72\,m_e$ and $0.86\,m_e$ for the directions of $(\Gamma \rightarrow Y)^0$, $(\Gamma \rightarrow Y)^{45}$ and $(\Gamma \rightarrow Y)^{60}$, respectively. The same trend is emerged in the case of the effective masses of holes. This means that the transfer of the carriers along the direction of $(\Gamma \rightarrow Y)$ is more likely to occur due to the lightest effective masses. This direction is identical to the orientation of the interface between the ZBNM and

ZGM units. Our result is in consistent with the experimental data reported by Ci et al.,[26] who claimed that the reduced electron and hole mobility can be attributed to the electron scattering at the boundaries between h-BN and graphene domains. As a result, the direction applied in the bandgap engineering is perpendicular to the direction of the carrier transfer, which may put forward to the complex application.

At last we turn our attention to the hybridized configurations with the different ratios of ZBNM and ZGM units, which are based on the $(ZBNM)_{10}$-$(ZGM)_{10}$ monolayer mentioned above [Figure 3]. Figure 5(a) – 5(d) shows the evolution of the calculated band structures for $(ZBNM)_2$-$(ZGM)_{18}$, $(ZBNM)_4$-$(ZGM)_{16}$, $(ZBNM)_6$-$(ZGM)_{14}$, and $(ZBNM)_8$-$(ZGM)_{12}$, respectively. In addition, the calculated energy gaps and magnetic moments are shown in Table 1 (Col^b). When the ratio of the ZGM units increase, the hybridized heterostructures still maintain the natures of metal at first. As the ratio reaches 2:18, the bandgap is opened anew with a value of 0.14 eV, indicating semiconducting nature of the $(ZBNM)_2$-$(ZGM)_{18}$. For $(ZBNM)_{12}$-$(ZGM)_8$, $(ZBNM)_{14}$-$(ZGM)_6$, $(ZBNM)_{16}$-$(ZGM)_4$, and $(ZBNM)_{18}$-$(ZGM)_2$, shown in Figure 5(e) – 5(h), the occurrence of transition is also been observed, while the valence band maximum (VBM) and conduction band minimum (CBM) both located near the Y point. Specifically, we find that the bandgap opens gradually by increasing the ratio of ZBNM units. The results also reveal the transition between the magnetic phase and the nonmagnetic occurs, while the ratios rise from 12:8 to 14:6. For the $(ZBNM)_{14}$-$(ZGM)_6$ [Figure 5f], the majority and minority protections of the spin are shown symmetric, leaving a tiny bandgap near the Fermi level. More interesting, in

the case of $(ZBNM)_{16}$-$(ZGM)_4$ [Figure 5g], the half-semimetallic character[45] is noticed, with an apparent energy gap for the minority projections of the spin, and two bands that seem to cross the Fermi level for majority projections of the spin. The crossing is not allowed by symmetry because each sublattice of C atoms is linked either to B or N, breaking equivalency of the sublattice and giving a tiny gap also for the majority projections of the spin bands. Hence, the term half-semimetal is more appropriate than half-metal commonly used in the literature. Here, the bandgaps of such hybridized configurations are further examined with the Heyd-Scuseria-Ernzerhof (HSE06) hybrid functional.[46] Based on our tests, we find that the HSE functional only enlarges the bandgaps moderately compared with the PBE but does not change the trend of electronic structure. Additionally, it is known to all that the bandgaps would be slightly overestimated by HSE06 while underestimated by PBE.[47, 48] Therefore, further experimental studies are of necessary. Further to increase the ratio of ZBNM units, we obtain the in-plane heterostructure of $(ZBNM)_{18}$-$(ZGM)_2$ with a bandgap of ~0.7 eV. These observations collectively demonstrate that the bandgap engineering and the transition from metal to half-semimetallic, and to semiconductor could also be realized by adjusting the ratios of the ZBNM and ZGM units.

4 Conclusion

In summary, a systematically study for the 2D in-plane heterostructures constructed by the ZBNM and ZGM units has been performed by means of first-principles calculations to engineer the electronic properties of such hybridized monolayers with

different ways. Our findings can be summarized into main points:

(1) The considered in-plane heterostructures in this work all show an ideal planar nature without any distortions. The connected ZBNM and ZGM units also maintain the symmetries and honeycomb-like structure.

(2) Our results show that the bandgap of the hybridized $(ZBNM)_m$-$(ZGM)_n$ monolayers can be tuned efficiently not only by adjusting the numbers of ZBNM and ZGM units with the same ratios, but also by changing the ratios of the different units.

(3) The character transition from insulator through semiconductor, and to metal can be realized via the variation of the numbers or the ratios of the ZBNM and ZGM units which are used to fabricate the in-plane heterostructures. Furthermore, we find the $(ZBNM)_{16}$-$(ZGM)_4$ displays a half-semimetallic character which would be favored in the applications of spintronics.

(4) In addition, the evaluation of the external strain for $(ZBNM)_2$-$(ZGM)_2$ demonstrates that the bandgap can be efficiently engineered by the tensile or compression strain, which mostly originates from the effect on the Y-axis.

(5) The discussion of the carrier effective mass reveals the transfer of charge carriers along the direction of $(\Gamma \rightarrow Y)$ is more likely to occur due to the smallest effective mass. Thus, the direction applied in the bandgap engineering by strain modulation is different from that of the carrier transfer, which will be convenient for further complex applications.

In a word, our results demonstrate the proposed ways are practical in engineering the

electronic properties of the studied configurations. Further experimental studies are expected to confirm the attractive predictions.

Acknowledgement

This work is supported by the National Basic Research Program of China (973 program, 2013CB632401), National Science foundation of China under Grants 21333006, 11374190, 11404187 and 111 Project B13029. We also thank the High Performance Computing Centre of Shandong University for providing high performance computation.

Notes and references

1. Geim, A. K.; Novoselov, K. S. *Nat. Mater.* **2007,** 6, 183-91.

2. Novoselov, K. S.; Geim, A. K.; Morozov, S. V.; Jiang, D.; Zhang, Y.; Dubonos, S. V.; Grigorieva, I. V.; Firsov, A. A. *Science* **2004,** 306, 666-9.

3. Novoselov, K. S.; Geim, A. K.; Morozov, S. V.; Jiang, D.; Katsnelson, M. I.; Grigorieva, I. V.; Dubonos, S. V.; Firsov, A. A. *Nature* **2005,** 438, 197-200.

4. Lee, C.; Wei, X.; Kysar, J. W.; Hone, J. *Science* **2008,** 321, 385-8.

5. Ma, Y.; Dai, Y.; Guo, M.; Huang, B. *Phys. Rev. B* **2012,** 85, 235448.

6. Berger, C.; Song, Z.; Li, X.; Wu, X.; Brown, N.; Naud, C.; Mayou, D.; Li, T.; Hass, J.; Marchenkov, A. N.; Conrad, E. H.; First, P. N.; de Heer, W. A. *Science* **2006,** 312, 1191-6.

7. Huard, B.; Sulpizio, J. A.; Stander, N.; Todd, K.; Yang, B.; Goldhaber-Gordon, D. *Phys. Rev. Lett.* **2007,** 98, 236803.

8. Bellido, E. P.; Seminario, J. M. *J. Phys. Chem. C* **2012,** 116, 8409-8416.

9. Jin, C.; Lin, F.; Suenaga, K.; Iijima, S. *Phys. Rev. Lett.* **2009,** 102, 195505.

10. Okamoto, H.; Kumai, Y.; Sugiyama, Y.; Mitsuoka, T.; Nakanishi, K.; Ohta, T.; Nozaki, H.; Yamaguchi, S.; Shirai, S.; Nakano, H. *J. Am. Chem. Soc.* **2010,** 132, 2710-8.

11. Radisavljevic, B.; Radenovic, A.; Brivio, J.; Giacometti, V.; Kis, A. *Nat. Nanotechnol.* **2011,** 6, 147-50.

12. Vogt, P.; De Padova, P.; Quaresima, C.; Avila, J.; Frantzeskakis, E.; Asensio, M. C.; Resta, A.; Ealet, B.; Le Lay, G. *Phys. Rev. Lett.* **2012,** 108, 155501.

13. Corso, M.; Auwarter, W.; Muntwiler, M.; Tamai, A.; Greber, T.; Osterwalder, J. *Science* **2004,** 303, 217-20.

14. Arnaud, B.; Lebegue, S.; Rabiller, P.; Alouani, M. *Phys. Rev. Lett.* **2006,** 96, 026402.

15. Golberg, D.; Bando, Y.; Huang, Y.; Terao, T.; Mitome, M.; Tang, C.; Zhi, C. *ACS Nano* **2010,** 4, 2979-93.

16. Song, L.; Ci, L.; Lu, H.; Sorokin, P. B.; Jin, C.; Ni, J.; Kvashnin, A. G.; Kvashnin, D. G.; Lou, J.; Yakobson, B. I.; Ajayan, P. M. *Nano Lett.* **2010,** 10, 3209-15.

17. Zeng, H.; Zhi, C.; Zhang, Z.; Wei, X.; Wang, X.; Guo, W.; Bando, Y.; Golberg, D. *Nano Lett.* **2010,** 10, 5049-55.

18. Al-Mashat, L.; Shin, K.; Kalantar-zadeh, K.; Plessis, J. D.; Han, S. H.; Kojima, R. W.; Kaner, R. B.; Li, D.; Gou, X.; Ippolito, S. J.; Wlodarski, W. *J. Phys. Chem. C* **2010,** 114, 16168-16173.

19. Rao, G.; Freitag, M.; Chiu, H. Y.; Sundaram, R. S.; Avouris, P. *ACS Nano* **2011,** 5, 5848-54.

20. Balog, R.; Andersen, M.; Jorgensen, B.; Sljivancanin, Z.; Hammer, B.; Baraldi, A.; Larciprete, R.; Hofmann, P.; Hornekaer, L.; Lizzit, S. *ACS Nano* **2013,** 7, 3823-32.

21. Topsakal, M.; Gürel, H. H.; Ciraci, S. *J. Phys. Chem. C* **2013,** 117, 5943-5952.

22. Levendorf, M. P.; Kim, C. J.; Brown, L.; Huang, P. Y.; Havener, R. W.; Muller, D. A.; Park, J. *Nature* **2012,** 488, 627-32.

23. Liu, Z.; Ma, L.; Shi, G.; Zhou, W.; Gong, Y.; Lei, S.; Yang, X.; Zhang, J.; Yu, J.; Hackenberg, K. P.; Babakhani, A.; Idrobo, J. C.; Vajtai, R.; Lou, J.; Ajayan, P. M. *Nat. Nanotechnol.* **2013,** 8, 119-24.

24. Huang, C.; Wu, S.; Sanchez, A. M.; Peters, J. J.; Beanland, R.; Ross, J. S.; Rivera, P.; Yao, W.; Cobden, D. H.; Xu, X. *Nat. Mater.* **2014,** 13, 1096-101.

25. Liu, L.; Park, J.; Siegel, D. A.; McCarty, K. F.; Clark, K. W.; Deng, W.; Basile, L.; Idrobo, J. C.; Li, A. P.; Gu, G. *Science* **2014,** 343, 163-7.

26. Ci, L.; Song, L.; Jin, C.; Jariwala, D.; Wu, D.; Li, Y.; Srivastava, A.; Wang, Z. F.; Storr, K.; Balicas, L.; Liu, F.; Ajayan, P. M. *Nat. Mater.* **2010,** 9, 430-5.

27. Liu, M.; Li, Y.; Chen, P.; Sun, J.; Ma, D.; Li, Q.; Gao, T.; Gao, Y.; Cheng, Z.; Qiu, X.; Fang, Y.; Zhang, Y.; Liu, Z. *Nano Lett.* **2014,** 14, 6342-7.

28. Kresse, G. *Phys. Rev. B* **1996,** 54, 11169-11186.

29. Kresse, G.; Joubert, D. *Phys. Rev. B* **1999,** 59, 1758-1775.

30. Perdew, J. P.; Burke, K.; Ernzerhof, M. *Phys. Rev. Lett.* **1996,** 77, 3865-3868.

31. Monkhorst, H. J.; Pack, J. D. *Phys. Rev. B* **1976,** 13, 5188-5192.

32. Ma, Y.; Dai, Y.; Guo, M.; Niu, C.; Zhu, Y.; Huang, B. *ACS Nano* **2012,** 6, 1695-701.

33. Bhowmick, S.; Singh, A. K.; Yakobson, B. I. *J. Phys. Chem. C* **2011,** 115, 9889-9893.

34. Liu, Y.; Bhowmick, S.; Yakobson, B. I. *Nano Lett.* **2011,** 11, 3113-6.

35. Drost, R.; Uppstu, A.; Schulz, F.; Hamalainen, S. K.; Ervasti, M.; Harju, A.; Liljeroth, P. *Nano Lett.* **2014,** 14, 5128-32.

36. Naumov, I.; Bratkovsky, A. M.; Ranjan, V. *Phys. Rev. Lett.* **2009,** 102, 217601.

37. Ma, Y.; Dai, Y.; Guo, M.; Niu, C.; Yu, L.; Huang, B. *Nanoscale* **2011,** 3, 2301-6.

38. Zhong, X. L.; Yap, Y. K.; Pandey, R.; Karna, S. P. *Phys. Rev. B* **2011,** 83, 193403.

39. Ma, Y.; Dai, Y.; Guo, M.; Niu, C.; Zhang, Z.; Huang, B. *Phys. Chem. Chem. Phys.* **2012,** 14, 3651-8.

40. Bae, S. H.; Lee, Y.; Sharma, B. K.; Lee, H. J.; Kim, J. H.; Ahn, J. H. *Carbon* **2013,** 51, 236-242.

41. Choi, S. M.; Jhi, S. H.; Son, Y. W. *Phys. Rev. B* **2010,** 81, 081407.

42. Zhou, M.; Lu, Y.; Zhang, C.; Feng, Y. P. *Appl. Phys. Lett.* **2010,** 97, 103109.

43. Xue, K.; Xu, Z. *Appl. Phys. Lett.* **2010,** 96, 063103.

44. Ma, X.; Dai, Y.; Guo, M.; Huang, B. *ChemPhysChem* **2012,** 13, 2304-9.

45. Pruneda, J. M. *Phys. Rev. B* **2010,** 81, 161409.

46. Heyd, J.; Scuseria, G. E.; Ernzerhof, M. *J. Chem. Phys.* **2003,** 118, 8207.

47. Zhang, H.; Zhang, Y.-N.; Liu, H.; Liu, L.-M. *J. Mater. Chem. A* **2014,** 2, 15389-15395.

48. Kang, J.; Tongay, S.; Zhou, J.; Li, J.; Wu, J. *Appl. Phys. Lett.* **2013,** 102, 012111.

Table 1. The calculated energy gaps (eV) and magnetic moments (μ_B) of the studied systems. [a]Term: the configurations of $(ZBNM)_m$-$(ZGM)_n$ with $m = n$. [b]Term: the configurations of $(ZBNM)_m$-$(ZGM)_n$ with $m \neq n$.

Col[a]	E_g	M	Col[b]	E_g	M
$(ZBNM)_2$-$(ZGM)_2$	1.19	0	$(ZBNM)_2$-$(ZGM)_{18}$	0.14	0
$(ZBNM)_4$-$(ZGM)_4$	0.14	0	$(ZBNM)_4$-$(ZGM)_{16}$	--	0.11
$(ZBNM)_6$-$(ZGM)_6$	0.01	0	$(ZBNM)_6$-$(ZGM)_{14}$	--	0.06
$(ZBNM)_8$-$(ZGM)_8$	--	0.13	$(ZBNM)_8$-$(ZGM)_{12}$	--	0.09
$(ZBNM)_{10}$-$(ZGM)_{10}$	--	0.11	$(ZBNM)_{12}$-$(ZGM)_8$	--	0.11
$(ZBNM)_{12}$-$(ZGM)_{12}$	--	0.10	$(ZBNM)_{14}$-$(ZGM)_6$	0.01	0
$(ZBNM)_{14}$-$(ZGM)_{14}$	--	0.10	$(ZBNM)_{16}$-$(ZGM)_4$	--	0
$(ZBNM)_{16}$-$(ZGM)_{16}$	--	0.16	$(ZBNM)_{18}$-$(ZGM)_2$	0.71	0

Table 2. Effective masses of electron (m_e^*) and hole (m_h^*) in the unit of free-electron mass for the $(ZBNM)_2$-$(ZGM)_2$ obtained from parabolic fitting to the CBM and VBM along selected direction in the reciprocal space

	Direction		
	$(\Gamma \rightarrow Y)^0$	$(\Gamma \rightarrow Y)^{45}$	$(\Gamma \rightarrow Y)^{60}$
m_e^*	0.6536	0.7182	0.8603
m_h^*	0.9219	1.1317	1.1661

Figure captions:

Figure 1. Top view of the atomic geometric configurations of the two dimensional in-plane heterostructures of h-BN and graphene monolayer. The dashed rectangle denotes the unit cell of the system. The orange, green and dark blue wafer represent B, C and N atoms, respectively.

Figure 2. The calculated band structures: (a) - (f) correspond to $(ZBNM)_2$-$(ZGM)_2$, $(ZBNM)_4$-$(ZGM)_4$, $(ZBNM)_6$-$(ZGM)_6$, $(ZBNM)_8$-$(ZGM)_8$, $(ZBNM)_{10}$-$(ZGM)_{10}$, $(ZBNM)_{12}$-$(ZGM)_{12}$, $(ZBNM)_{14}$-$(ZGM)_{14}$, and $(ZBNM)_{16}$-$(ZGM)_{16}$, respectively. The solid (blue) and dotted (red) curves correspond to spin-up and spin-down states, respectively. The black dash curve stands for Fermi level, and the Fermi level is set to be zero.

Figure 3. The top (a) and side (b) views of the spin density isosurface (isosurface value = 0.01) for the $(ZBNM)_{10}$-$(ZGM)_{10}$ monolayer. Yellow (cyan) indicates the positive (negative) values.

Figure 4. The effect of strain on bandgap of the $(ZBNM)_2$-$(ZGM)_2$ monolayer E_g (in eV). In the inset, we show the X-axis and Y-axis direction where the strain is applied

along. The black, green and red lines show the variation in the energy bandgap (in eV) under biaxial, X-axis and Y-axis strain deformation, respectively.

Figure 5. Band structure close to the Fermi level (horizontal dashed line) of (a) $(ZBNM)_2$-$(ZGM)_{18}$, (b) $(ZBNM)_4$-$(ZGM)_{16}$, (c) $(ZBNM)_6$-$(ZGM)_{14}$, (d) $(ZBNM)_8$-$(ZGM)_{12}$, (e) $(ZBNM)_{12}$-$(ZGM)_8$, (f) $(ZBNM)_{14}$-$(ZGM)_6$, (g) $(ZBNM)_{16}$-$(ZGM)_4$, (h) $(ZBNM)_{18}$-$(ZGM)_2$. The drake blue line and the red dashed line represent the spin-up and spin-down states, respectively. The B, C and N atoms are highlighted in orange, green and dark blue, respectively.

Figure 1. Top view of the atomic geometric configurations of the two dimensional in-plane heterostructures of h-BN and graphene monolayer. The dashed rectangle denotes the unit cell of the system. The orange, green and dark blue wafer represent B, C and N atoms, respectively.

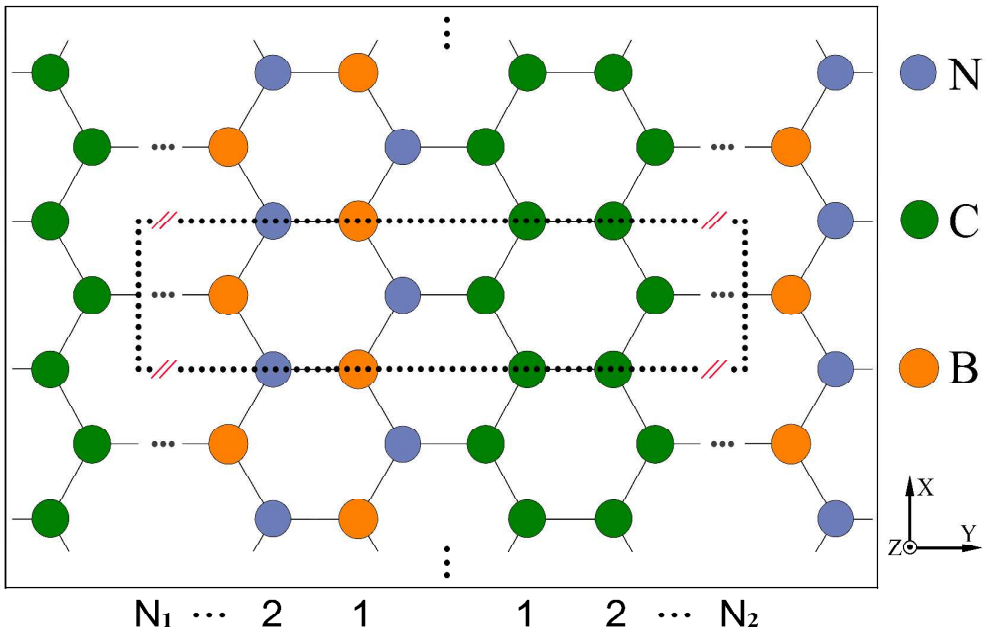

Figure 2. The calculated band structures: (a) - (h) correspond to $(ZBNM)_2$-$(ZGM)_2$, $(ZBNM)_4$-$(ZGM)_4$, $(ZBNM)_6$-$(ZGM)_6$, $(ZBNM)_8$-$(ZGM)_8$, $(ZBNM)_{10}$-$(ZGM)_{10}$, $(ZBNM)_{12}$-$(ZGM)_{12}$, $(ZBNM)_{14}$-$(ZGM)_{14}$, and $(ZBNM)_{16}$-$(ZGM)_{16}$, respectively. The solid (blue) and dotted (red) curves correspond to spin-up and spin-down states, respectively. The black dash curve stands for Fermi level, and the Fermi level is set to be zero.

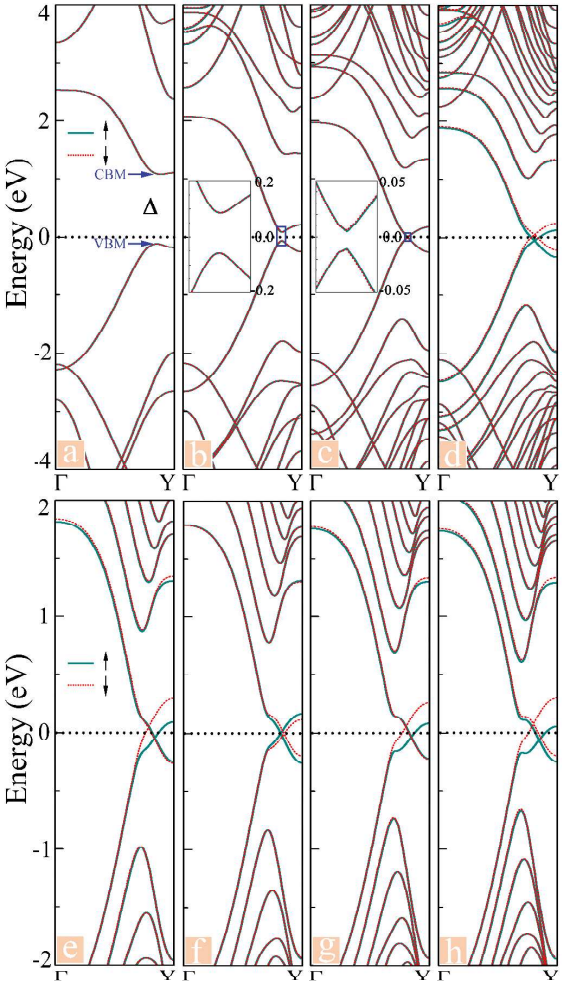

Figure 3. The top (a) and side (b) views of the spin density isosurface (isosurface value = 0.01) for the $(ZBNM)_{10}$-$(ZGM)_{10}$ monolayer. Yellow (cyan) indicates the positive (negative) values.

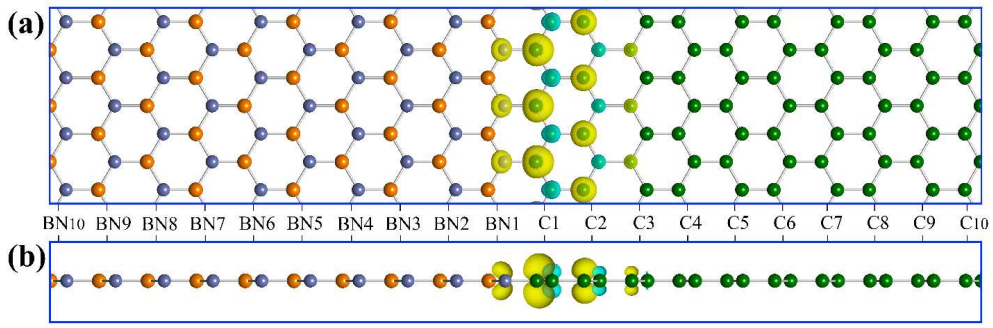

Figure 4. The effect of strain on bandgap of the $(ZBNM)_2$-$(ZGM)_2$ monolayer E_g (in eV). In the inset, we show the X-axis and Y-axis direction where the strain is applied along. The black, green and red lines show the variation in the energy bandgap (in eV) under biaxial, X-axis and Y-axis strain deformation, respectively.

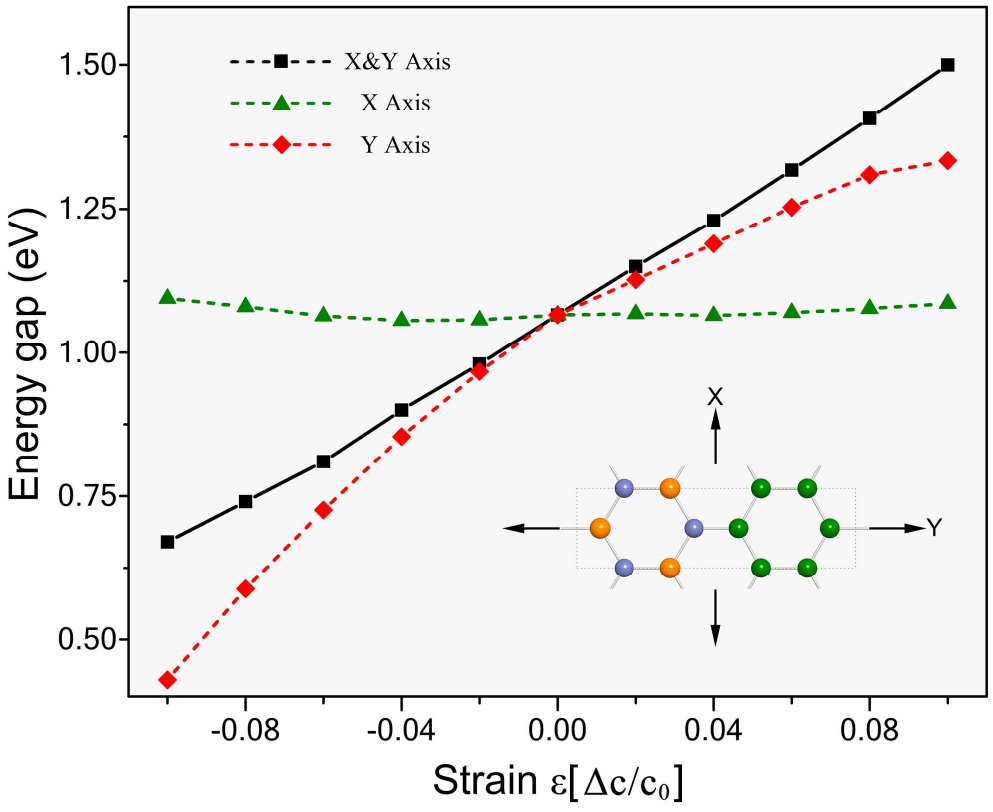

Figure 5. Band structure close to the Fermi level (horizontal dashed line) of (a) $(ZBNM)_2$-$(ZGM)_{18}$, (b) $(ZBNM)_4$-$(ZGM)_{16}$, (c) $(ZBNM)_6$-$(ZGM)_{14}$, (d) $(ZBNM)_8$-$(ZGM)_{12}$, (e) $(ZBNM)_{12}$-$(ZGM)_8$, (f) $(ZBNM)_{14}$-$(ZGM)_6$, (g) $(ZBNM)_{16}$-$(ZGM)_4$, (h) $(ZBNM)_{18}$-$(ZGM)_2$. The drake blue line and the red dashed line represent the spin-up and spin-down states, respectively. The B, C and N atoms are highlighted in orange, green and dark blue, respectively.